JOURNAL OF SYNCHROTRON RADIATION

ISSN 1600-5775

Nanoscale element behavior in a continuum

Sungsook Ahn[a]* and Sang Joon Lee[b]

[a]Berkeley Laboratory, Berkeley, CA 94720, USA, and [b]Department of Mechanical Engineering, Pohang University of Science and Technology, Pohang 37673, Republic of Korea. *Correspondence e-mail: sungsookahn@yahoo.com

Received 8 February 2020
Accepted 19 May 2020

Edited by A. F. Craievich, University of São Paulo, Brazil

Keywords: nanocomposites; stimuli-responsiveness; patterns; wrinkles; X-ray imaging.

Supporting information: this article has supporting information at journals.iucr.org/s

Patterns in materials are not just decoration but also important for function. In view of this, the dynamics of patterning procedures in materials has been investigated as an important developmental procedure. In this study, nanoscale components in a continuum are traced in terms of natural patterning procedures. Externally applied compressive or extensive forces to an elastic thin sheet commonly induce an orientated lateral line pattern. From a nanoscale element point of view, the dynamics of natural arrangements, forming anisotropic patterns in preference to isotropy, still remains unclear. In this study, new developmental procedures for line patterns are suggested by stimuli-responsive viscoelastic nanocomposite network model systems. Forces originating from an internal source without directional orientation generate lines in preference to isotropic patterns. With repeated, non-oriented (or isotropic) and self-modulated strain variations, stress is accumulated to drive anisotropic orientations and further lines. The anisotropic elemental arrangement is justified by the equilibrium between the short-range attraction and long-range repulsion from a bottom-up viewpoint. This study suggests a new material design methodology that is useful for electrical devices, biomedical devices and other patterned soft condensed matter in conjunction with line patterns typically generated in a broad range of viscoelastic materials.

1. Introduction

Natural patterning procedures shed light on material design and fabrication methodology in an energy efficient way. Naturally occurring dynamic transformation procedures result in characteristic patterns in geology (Mariotti *et al.*, 2014), biology (Summers *et al.*, 2013) and material science (Koo *et al.*, 2010). In terms of patterning dynamics, the Fibonacci sequence (Li *et al.*, 2005), golden ratio (Livio, 2003), fractals (Falconer, 2014), self-similarity (Ostling *et al.*, 2000), recursion (https://www.cs.berkeley.edu/~bh/ssch14/recur-patterns.html, accessed May 2020) and symmetry (Golubitsky *et al.*, 1999) have been conceptualized and some have been theoretically accessed by reaction-diffusion mechanisms (http://www.rsc.org/chemistryworld/2012/05/turing-patterns, accessed May 2020; Maini *et al.*, 2006; Kondo & Miura, 2010). Morphogenesis of soft tissues, wrinkling of skin (Cerda & Mahadevan, 2003; Efimenko *et al.*, 2005), fingerprint formation (Bae *et al.*, 2015) and convolution of brains (Richman *et al.*, 1975) originate from dynamic patterning mechanisms.

The dynamics of directional ordering eventually result in anisotropic line patterns (Sillitoe, 1974; Mortensen & Suresh, 1995; Freitas *et al.*, 1994). In a broad range of natural and artificial systems, a self-directed force propagates from an internal source of a deformable body, which is non-specific in orientation, repetitive in periodicity and self-modulated in strength. However, the patterning origins and developmental procedures of the anisotropic arrangement, preferable over

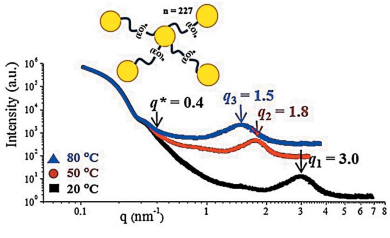

isotropy, have not yet been clarified. Soft materials are deformable and succumb to instabilities of highly nonlinear modes of anisotropic patterns such as creases (Hohlfeld, 2008), folds (Pocivavsek *et al.*, 2008) and ridges (Cao & Hutchinson, 2012). When the bilayer structure of a stiff thin film on a compliant thick substrate is compressed by a critical load, wrinkles set in to release stress in a finite space. The wavelength of the wrinkles is determined by the balance between the deformation of the substrate, which favors short wavelengths, and the bending of the film, which favors long wavelengths (Cerda & Mahadevan, 2003; Huang *et al.*, 2005; Chen & Hutchinson, 2004; Danov *et al.*, 2010). When the loading is uniaxial, parallel wrinkles occur perpendicular to the compression direction (Efimenko *et al.*, 2005). Meanwhile, when the loading is biaxial, complex modes of wrinkles are observed (Yin *et al.*, 2012), such as herringbone, checkerboard and hexagonal. Wrinkles are also formed under tensile stretching (Cerda *et al.*, 2002), shearing (Ciarletta *et al.*, 2013) and bending (Destrade *et al.*, 2010). Different from these, the use of anisotropic shapes or directional interactions of free particulates (Fejer *et al.*, 2011; Sciortino *et al.*, 2007) and other non-equilibrium procedures (Rabani *et al.*, 2003; Gupta *et al.*, 2006; Kammler *et al.*, 2004; Ogawa *et al.*, 2000) have been reported as direct strategies to create anisotropic assemblies in terms of the initial anisotropic arrangement. Nonetheless, how the elemental components in a continuum are anisotropically arranged, which further leads to wrinkle patterns, has not been clearly explored.

In this study, the dynamic origin of the anisotropic arrangement is investigated by using temperature-responsive nanocomposite model systems in which the cyclic repetition of volume change of a continuum is designed. This volume change repetition is a popular phenomenon of materials. A strain is self-modulated through the temperature-responsiveness of the designed nanocomposites without externally applied mechanical forces. This design reproduces natural dynamics to explain the line pattern formation that occurs in a broad range of natural and artificial systems. In addition to sufficient energy to deform a material, how non-directionally actuated forces eventually generate directionally elongated line patterns is discussed from a bottom-up viewpoint (Belkin *et al.*, 2007; Seul & Andelman, 1995; Tang *et al.*, 2006). To the best of our knowledge, this is the first study of the nanocomponent contribution to line pattern formation dynamics. These natural thus effective (possibly energy-efficient) nanoscale patterns would be highly useful for advanced control methodology for various soft elastic materials.

2. Results and discussion

2.1. Model system design: temperature-responsive nanocomposites

The responsiveness of a material is induced by the solubility and conformational transition of molecules triggered by external stimuli (Ahn *et al.*, 2008, 2009). In this study a model system is designed with a temperature-responsive network in water (hydrogel) in which branched polyethylene glycol (PEG) is multiply linked on a gold nanoparticle (AuNP) (Fig. S1A of the supporting information) (Ahn & Lee, 2014, 2015). The molecular weight between the junction points (M_p) and branch structure is controlled by di-functional 2PEG3400 and 2PEG10000 as well as tetra-functional 4PEG10000 and 4PEG20000. This generates a proper *in situ* responsiveness with minimum fatigue during measurement by small-angle X-ray scattering (SAXS) under the designed conditions. The observed SAXS peaks are dominated by the PEG polymers interlinking the AuNPs and determine the correlation length of the nanocomposite network. The peaks in the SAXS profiles generated from AuNPs and their cluster are out of the observation range. The designed amount of thiol functionalized PEG aqueous solution is mixed with prepared AuNPs of 2 nm average diameter (2.4×10^{21} AuNPs m^{-3}) followed by purification to remove unreacted PEGs and AuNPs by membrane dialysis (Cellulose Ester, MW 20KDa cut, Spectra/Por®). The concentration of the PEG is varied from five times the number of AuNPs (×5). Depending on this number ratio of PEGs to AuNPs (×10 or ×20), the structures are diversified, which is indicated by the q values of the SAXS profiles (Fig. S2).

The structural changes of the selected 2PEG10000 nanocomposite hydrogel are investigated by SAXS in hierarchical length scales between 20°C and 80°C temperature stimuli [Fig. 1(*a*)]. Under the designed experimental conditions,

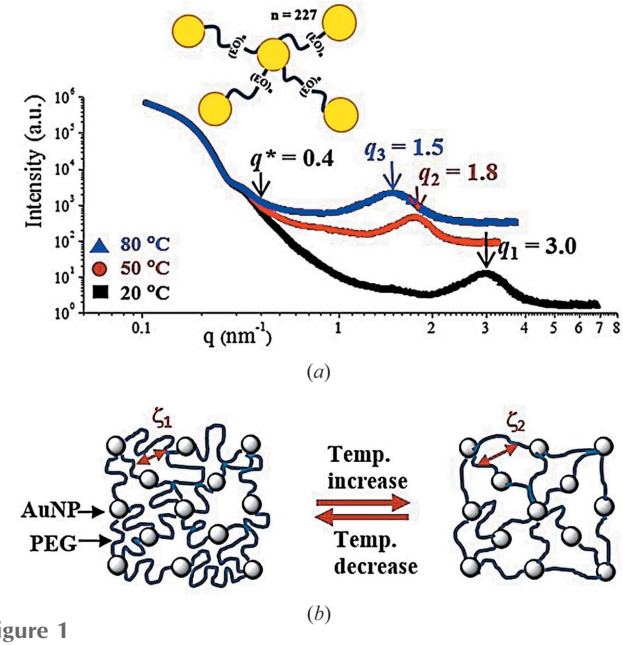

Figure 1
(*a*) Temperature responsiveness of the designed AuNP 2PEG10000 nanocomposite hydrogel obtained by SAXS. The structural changes are investigated in hierarchical length scales between 20°C and 80°C. The PEG chains in the nanocomposites are stretched and realigned within a frame, determined by q^* (~0.4 nm^{-1}). This is the end-point below which there is no more structural change. By the peak positions q_1 (20°C), q_2 (50°C) and q_3 (80°C) the average correlation length (ζ) is compared. (*b*) Schematic illustration of the correlation length (ζ) change driven by the temperature changes between lower (ζ_1) and higher (ζ_2) states. Due to chain shrinkage at higher temperature, $\zeta_1 < \zeta_2$ is satisfied.

structural change is completed without any intermediate under a repeated temperature switch. As a typical feature of a soft responsive material, the PEG chains in the nanocomposites are stretched and realigned within a frame of size determined by q^* ($\sim$0.4 nm^{-1}) of the SAXS profiles; q^* indicates the end-point above which size scale there is no further structural change. The average correlation length is compared at different temperatures and is inversely proportional to the peak position. At 20°C, the main peak position is around q_1 = 3 nm^{-1} and moves to q_2 = 1.8 nm^{-1} at 50°C and further to q_3 = 1.5 nm^{-1} at 80°C. Therefore, driven by the lower critical solution temperature property of PEGs (Ahn *et al.*, 2010; Ahn & Lee, 2014, 2015), the correlation length (ζ) of the designed nanocomposites increases at an increased temperature for shrunken PEGs, while it decreases at a decreased temperature for swollen PEGs ($\zeta_1 < \zeta_2$) [Fig. 1(*b*)].

2.2. Line pattern formation by volume change repetition (f)

A force is induced by a solubility change of the PEGs according to the temperature, thus the stress (σ) is self-modulated by the stimuli-responsiveness of the nanocomposite itself without externally applied physical forces. The spatial distribution of the AuNPs in the nanocomposite is traced by the contrast created by Au in X-ray nanoimaging (XN) (see *Methods* section). The collectively traced nodal position of the nanocomposite network is displayed by the XN images and schematic illustration of the representative AuNP distributions in the network [Fig. 2(*a*), top and bottom, respectively]. f is the number of heating–cooling cyclic repetitions between T_{min} = 20°C and T_{max} = 60°C (±1.5°) performed at 0.125 min^{-1} frequency under controlled humidity conditions of relative humidity (RH) = 75% to minimize water loss during the experiments. In the initial state at f = 0 the network nodes are homogeneously distributed, and at f = 10 the network nodes are clustered into an isotropic arrangement. However, at f = 20 the clusters start to elongate and line patterns become prominent at f = 50 and 70. This line patterning procedure is reproduced in a broad range of nanocomposite systems. The visco-elastic stress relaxation is considered in terms of the stored stress (σ). The stress relaxation modulus, $G(t)$, relaxes into a finite equilibrium shear modulus, $G_{eq} = G(t \rightarrow \infty)$. σ exponentially relaxes towards zero at and beyond the Maxwell time ($t \geq \tau_M$): $G(t) = G_M \exp(-t/\tau_M)$. At a specific time t_i before reaching τ_M ($t_i < \tau_M$), the modulus $G_M[1 - \exp(-t_i/\tau_M)]$ remains at each cycle and is stored up during the entire repetition procedures. If $G(t)$ is independently the same during the cyclic repetitions (f), the remaining modulus is accumulated step-by-step, $G_n(t) = \Sigma G_i(t) = \Sigma\{G_M[1 -$

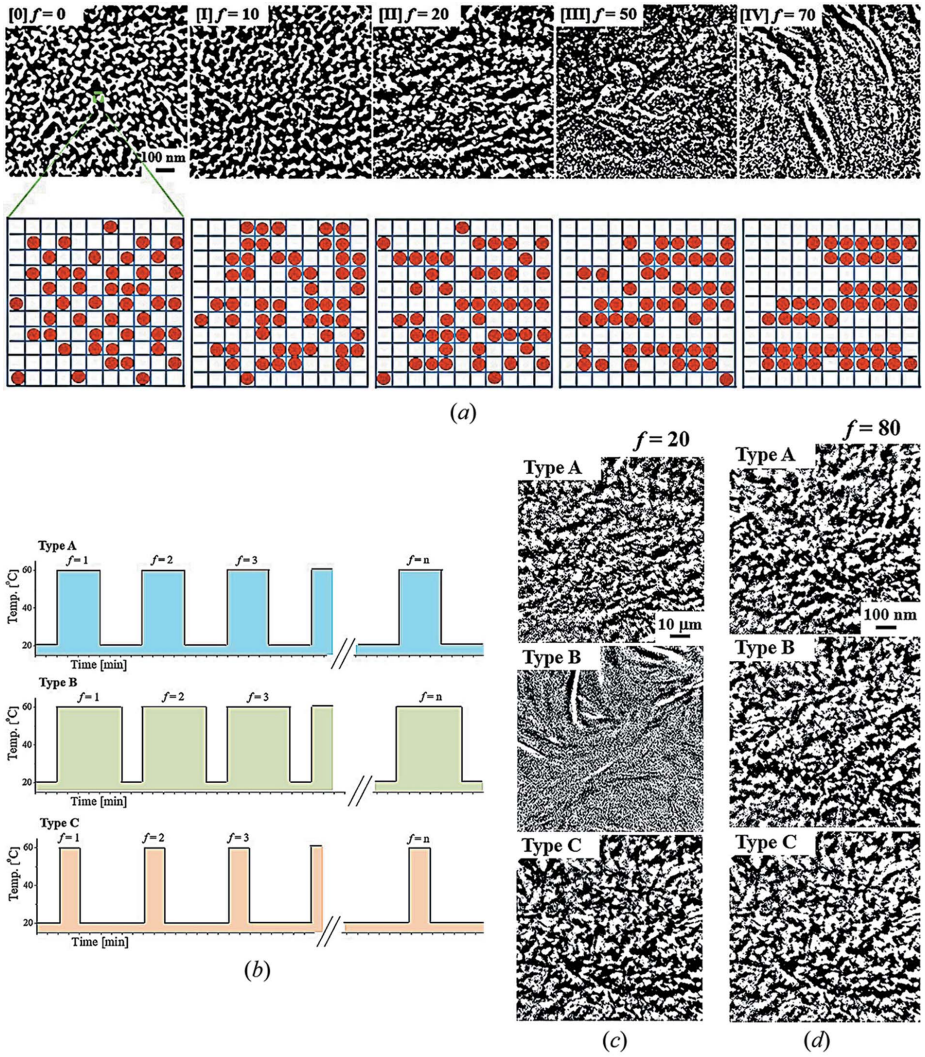

Figure 2
(*a*) XN images of the designed nanocomposite in accordance with the f value changes (top), and schematic illustration of the representative spatial distribution of AuNPs for each corresponding case (bottom). The repeated temperature starting from low temperature and then high temperature and then back to the original low temperature condition is defined as f = 1. AuNPs are homogeneously distributed at initial f = 0 [0] and form isotropic clusters at f = 10 [I]. However, the clusters elongate at f = 20 [II] and at f = 50 [III]. On further increase to f = 70 [IV], line formation becomes prominent. (*b*) Three types of temperature variation cycle at a fixed frequency of 0.125 min^{-1}. The transition temperature for change is short enough to be neglected. The Type A symmetric temperature variation is designed with 4 min at 60°C and 4 min at 20°C; the asymmetric Type B with 6 min at 60°C and 2 min at 20°C; and Type C with 2 min at 60°C and 6 min at 20°C. (*c*) XN images of the nanocomposites in accordance with the designed types at a fixed state of f = 20. Wrinkling is accelerated in Type B. (*d*) None of the types generates line patterns even at a high f = 80 when a small volume change is induced by the temperature shift between 20°C and 50°C.

$\exp(-t_i/\tau_M)]\}$ (i = 1, 2, 3, ..., n, $0 \le t_i \le t$) until n reaches the designed f.

2.3. Critical threshold strain (γ_{cr}) for line pattern formation

Based on the temperature-dependent structural information obtained in Fig. 1(*a*), a repeated structural change is designed. To examine the effects of the dynamic actuation in the networks, three heating–cooling cyclic repetition types (Types A, B and C) are compared in which the expansions and shrinkages of PEG chains are independently controlled keeping a 0.125 min^{-1} frequency [Fig. 2(*b*)]. For Type A, cyclic repetition is symmetric, 4 min at each temperature; for Type B, low temperature for 2 min and high temperature for 6 min; and for Type C, opposite to Type B, low temperature for 6 min and high temperature for 2 min. XN images of the nanocomposites at f = 20 repeating between 20°C and 60°C are compared under the three different heating–cooling actuation types [Fig. 2(*c*)]. The resultant images for Types A and C are almost the same, whereas Type B exhibits a prominent wrinkle pattern. Therefore, $G_n(t)$ is less dependent on the f value but is more strongly affected by the actuation type. Maintaining a low temperature in the chain relaxation state (full swelling) for a relatively short time, as applied for Type B, thus satisfies the condition $t_i < \tau_M$, by which a specific amount of modulus is stored. This contributes to a sufficient energy source for line pattern formation.

A thin elastic sheet of a certain geometry remains flat as long as the longitudinal stretching strain (γ) in its plane is smaller than the critical stretching strain ($\gamma < \gamma_c$) (Wagner, 1929; Mansfield, 1968; Steigmann, 1990). However, the sheet starts to buckle at the critical condition of $\gamma \simeq \gamma_c$ to accommodate the in-plane strain incompatibility by the Poisson effect (Ogawa *et al.*, 2000), while further stretching causes wrinkling ($\gamma > \gamma_c$). The nanocomposite structure at f = 80 repeating between 20°C and 50°C is displayed under the three different heating–cooling actuation types [Fig. 2(*d*)]. The result demonstrates that, even with a high f, none of the designed cyclic repetition types contributes to wrinkle formation when the temperature changes between 20°C and 50°C. The SAXS result [Fig. 1(*a*)] confirms that the degree of size change is proportional to the temperature change span. Only a sufficient degree of ζ size change induced by a sufficient temperature difference exclusively leads to wrinkle line formation. This suggests the existence of a critical threshold strain (γ_{cr}) that cannot be obtained only through the stress accumulation driven by the number of repetitions. Nonetheless, it can be explained in conjunction with the Mullins effect (https://abaqus-docs.mit.edu/2017/English/SIMACAEMATRefMap/simamat-c-mullins.htm) in which the stress–strain curve depends on the previously encountered maximum strain. γ is gradually accumulated to reach γ_c with increasing f. In addition, a viscoelastic modulus $G(t)$ on a sufficient amplitude of the strain ($\gamma \ge \gamma_{cr}$) is necessary. As a result, for wrinkle formation, f must be sufficiently large to reach γ_c and each γ_i should exceed the threshold value, $\gamma_c \simeq \Sigma\, \gamma_i f_i$ ($\gamma_i > \gamma_{threshold}$).

2.4. Network dynamics

The structure of the designed nanocomposites is actively diversified in a small-scale region ($q > q^*$) according to changes in temperature and f. The structural variations are induced with a symmetric heating and cooling repetition at 0.125 min^{-1} frequency (Type A) at the changes of f = 10 [I], f = 20 [II] and f = 50 [III] above the critical condition ($\Delta\zeta > \Delta\zeta_{critical}$) [Fig. 3(*a*)]. ζ increases with temperature increase due to PEG shrinkage {q_1 = 2.5 (20°C) > q_2 = 1.3 (80°C) at f = 10 [I] and q_1 = 2.1 (20°C) > q_2 = 1.1 (80°C) at f = 20 [II]}. An increase in f from 10 to 20 causes isotropic expansion of network arrangements (increase in ζ) detected by a q value decrease {q_1 = 2.5 (f = 10 [I]) > q_1 = 2.1 (f = 20 [II]) at 20°C and q_2 = 1.3 (f = 10 [I]) > q_2 = 1.1 (f = 20 [II]) at 80°C}. The structural distortion is relatively less significant until f = 20 [II] retaining one main SAXS peak. Meanwhile, from f = 50 [III] the nodal positions are significantly rearranged with a prominent change of q_i and q^* position as well as multiple peak generation at different length scales without structural correlation. Based on the SAXS result, the suggested structural changes are illustrated in Fig. 3(*b*). The two prominent ζ_{III} values are mixed at f = 50 [III]. Soft materials such as rubber and living tissues exhibit material softening under cyclic loading (Ogawa *et al.*, 2000; Zhuang & Halford (2001). This typical phenomenon is also directly induced in this study where an increase of f generally increases ζ of the designed networks.

The network models have been developed in relation to the junctions and chain structures of a network (see Section *Network models* in the supporting information). The ensemble average of the position vector $\langle \Delta X_i^2 \rangle$ is normalized by the mean-square fluctuation of the end-to-end distance $\langle x_0^2 \rangle$ at a point on a chain with a normalized length between the junctions ($0 \le \xi \le 1$). The nodal point fluctuation of a continuum affected by deformation is evaluated at a point on a chain ($0 \le \xi \le 1$) in the network model. The structural change of a continuum is a function of the deformation factor (λ), functionality (ϕ) and degree of fixation (κ). The location of the junction point is fixed in the Affine model, for which the normalized fluctuation is expressed as $\langle \Delta X_i^2 \rangle / \langle x_0^2 \rangle_{Affine}$ ($\kappa = \infty$). Meanwhile, the junction movement is maximized in the Phantom model as $\langle \Delta X_i^2 \rangle / \langle x_0^2 \rangle_{Phantom}$ ($\kappa = 0$). Between these two ideal network models, $\langle \Delta X_i^2 \rangle / \langle x_0^2 \rangle$ of the chains are evaluated according to the κ value change. $\langle \Delta X_i^2 \rangle / \langle x_0^2 \rangle$ at the middle of the chain (ξ = 0.5) increases with an increase in the volumetric deformation (λ^3), which increases by the increase in κ of the network after an intersection at each ϕ = 3 and 5 condition [Fig. 3(*c*)]. Even with the increase in ϕ from 3 to 5, the movement of the chain center (ξ = 0.5) is similar.

On the other hand, $\langle \Delta X_i^2 \rangle / \langle x_0^2 \rangle$ at the junction points (ξ = 0) is less dependent on the deformation (λ^3) overall [Fig. 3(*d*)]. Small κ values generate large $\langle \Delta X_i^2 \rangle / \langle x_0^2 \rangle$ values. Between the two almost flat ideal values, the normalized fluctuation of real chains ($0 < \kappa < \infty$) increases by λ^3. It is the opposite tendency to those at the chain center (ξ = 0.5). Thus the $\langle \Delta X_i^2 \rangle / \langle x_0^2 \rangle$ value increases with an increase of the junction freedom which is an inverse value of the degree of fixation ($1/\kappa$). With the

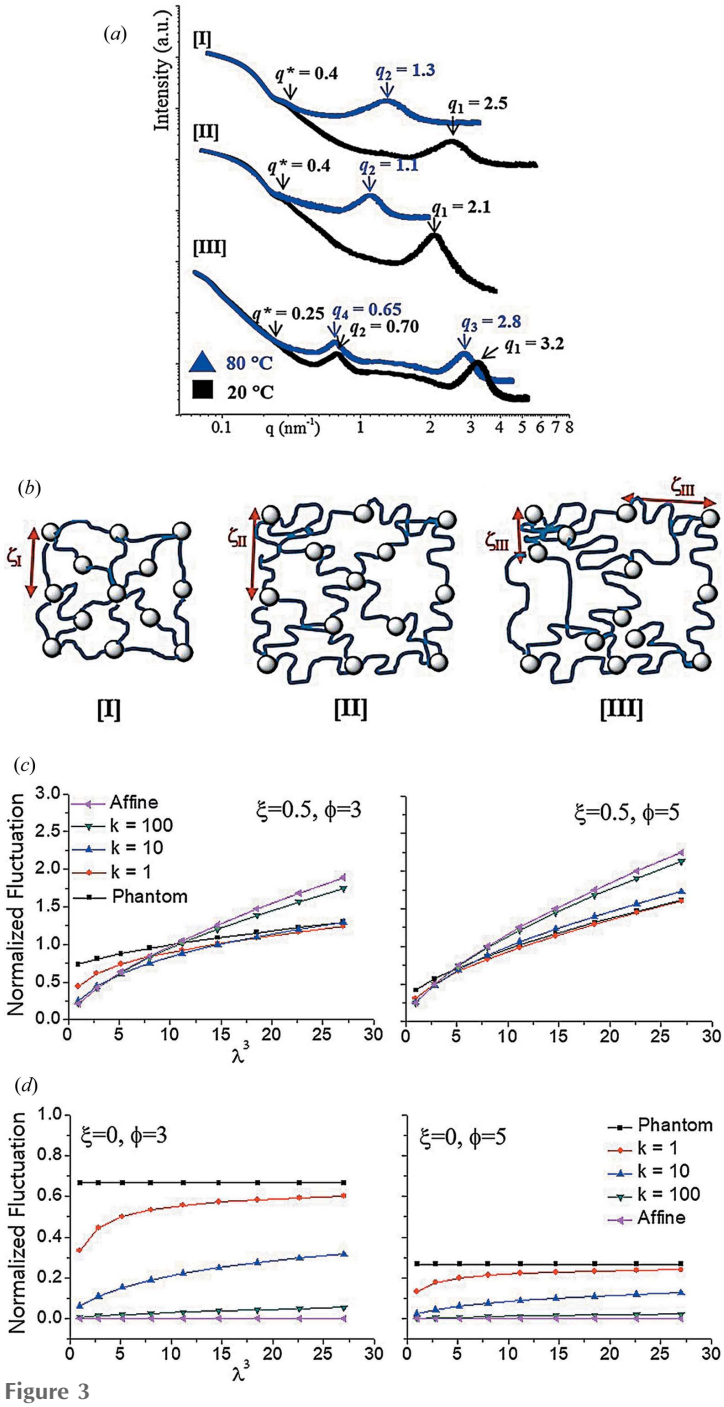

Figure 3
(*a*) SAXS results of the nanocomposite induced by a symmetric cyclic repetition at 0.125 min^{-1} frequency (Type A) by the changes of $f = 10$ [I], $f = 20$ [II] and $f = 50$ [III]. ζ increases as temperature increases ($q_1 > q_2$). An increase of f from 10 [I] to 20 [II] causes isotropic expansion of network arrangements detected by a q value decrease. The structural distortion is significant from $f = 50$ [III] with a prominent change of q_i position and q^* change as well as multiple peak generation. (*b*) The illustrated structural changes obtained by the SAXS results in (*a*). ζ increases as f increases from [I] to [II] ($\zeta_I < \zeta_{II}$). ζ_{III} is diversified because of structural complications and inhomogeneity in the whole nanocomposite network at $f = 50$ [III]. (*c*) Normalized fluctuation ($\langle \Delta X_i^2 \rangle / \langle x_0^2 \rangle$) versus volumetric deformation factor (λ^3) for each functionality, $\phi = 3$ and $\phi = 5$, at the middle point between the junctions, $\xi = 0.5$. The degree of fluctuation (κ) is varied between 1 and 100 compared with the two ideal model networks of Affine ($\kappa = \infty$) and Phantom ($\kappa = 0$). (*d*) Normalized fluctuation ($\langle \Delta X_i^2 \rangle / \langle x_0^2 \rangle$) versus volumetric deformation factor (λ^3) for each functionality, $\phi = 3$ and $\phi = 5$, at the junctions, $\xi = 0$.

increase of ϕ from 3 to 5, the movement of the junction point ($\xi = 0$) is significantly limited. The polymer chain center ($\xi = 0.5$) obtains more freedom to move around when the junctions are fixed (thus the total free energy is maintained).

2.5. Dynamics of AuNPs in the PEG networks

The experimental $\langle \Delta X_i^2 \rangle / \langle x_0^2 \rangle$ values at the junction points ($\xi = 0$) are evaluated and compared with ideal chains. The degree of interconnection is diversified by controlling the amount of bi-functional PEGs to AuNPs by ×5, ×10 and ×20 (Fig. S2). This diversifies the functionality (ϕ) and the degree of junction fixation (κ) of the whole network. The normalized fluctuations of the junctions ($\xi = 0$) are experimentally averaged by tracing the position changes of AuNPs in the XN images. It is related to λ^3 experimentally obtained by SAXS (assuming isotropic expansion, $\lambda \simeq 1/q_i$) according to the temperature and the f values. For the selected 2PEG10000 with ×5, ×10 and ×20 conditions, the experimental results are compared by normalized fluctuation versus λ^3 [Fig. 4(*a*)]. The normalized fluctuation values of the designed systems are between the two ideal models ($\kappa = 0$ for Phantom and $\kappa = 100$ for pseudo-Affine) with selected ϕ values of 3 and 10. The normalized fluctuation of ideal chains is almost independent of the degree of deformation (λ^3) of the whole network, while those of all the experimental systems significantly increase as λ^3. The increase of $\langle \Delta X_i^2 \rangle / \langle x_0^2 \rangle$ is more prominent for less cross-linked 2PEG with ×5, while it is smaller for more cross-linked 2PEG with ×20. The tendency of the result is matched with the theoretical evaluation performed from $\kappa = 1$ to 100 displayed in Fig. 3(*d*). From the network evaluation, two cooperating factors are suggested to control the junction movement. With proper junction freedom ($1/\kappa$) far from ideal conditions ($\kappa \neq 0$ or ∞), increasing the network deformation (λ^3) increases the junction movement. However, increasing the chain freedom by responsiveness limits the junction movement which is more restricted by high functionality (ϕ). In the selected XN images, the collective behaviors of AuNPs in the nanocomposites are displayed and the corresponding images are magnified [Fig. 4(*b*)]. Along with an increase in ϕ (×5, ×10 and ×20), the junction points range from an isotropic distribution to an elongated arrangement at a fixed f (= 20). AuNPs form non-directionally distributed clusters at low ϕ (×5). However, those clusters are oriented into lines (×10), which are further congested into prominently connected anisotropic lines (×20).

Driven by the hydrophobic force, an increase in hydrophobicity and volume fraction of amphiphilic molecules generates a sequence of self-assembled structures from isotropic to elongated cylindrical micelles. The observed structural sequence is similar to this typical self-assembly procedure. The bottom-up line pattern formation is explained by tracking the arrangements of indivi-

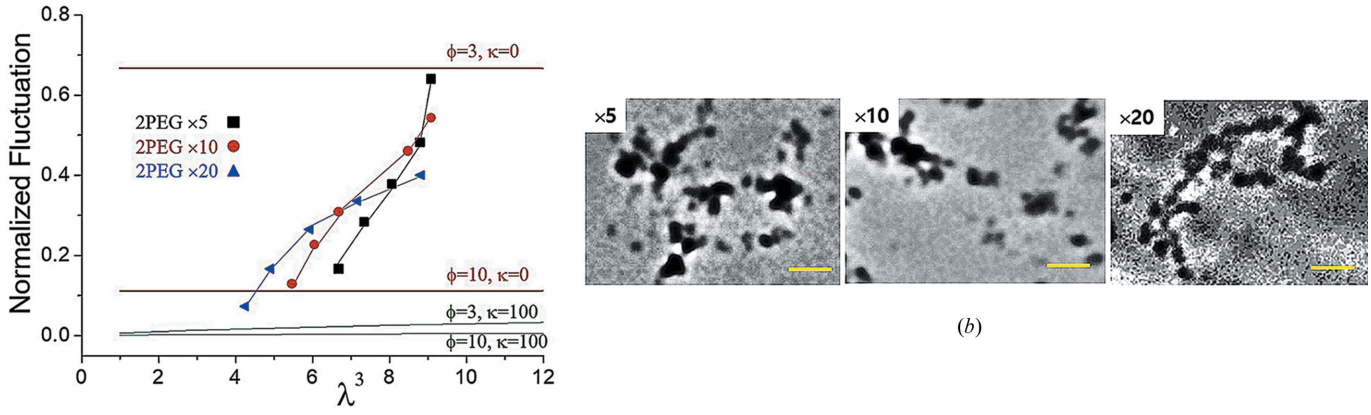

Figure 4
(*a*) Experimentally obtained normalized fluctuation ($\langle \Delta X_i^2 \rangle / \langle x_0^2 \rangle$) versus volumetric deformation factor (λ^3) are evaluated with the pseudo Affine (κ = 100) and Phantom (κ = 0) models at the selected ϕ = 3 and 10. The degree of interconnection is diversified by controlling the amount of binary thiol end-capped functional PEGs (a fixed M_p = 10000) to the AuNP by ×5, ×10 and ×20. (*b*) Collective behaviors of AuNPs in the nanocomposites obtained by XN image. The degree of connectivity is controlled by ×5, ×10 and ×20 at a fixed f = 20. The scale bar is 10 nm The images show bottom-up line pattern formation.

dual AuNPs with increasing ϕ. This cooperative interaction supports the anisotropic arrangement of nanoscale elements. In addition, consequently ϕ and f determine the line pattern formation in a bottom-up viewpoint. Before it reaches a critical condition {Fig. 3(*a*) stage [III]}, increase of f at a fixed ϕ contributes to increased λ, leading to acceleration of the line pattern formation. On the other hand, an increased ϕ also contributes to bottom-up line pattern formation at a certain f; this might be caused by a limitation in junction movements. The whole network system naturally expands by swelling–deswelling dynamics as long as the structure permits; this is limited by chemically linked structure. At this point, the bottom-up line pattern formation is explained by an equilibrium between a spatial expansion and a limitation.

2.6. Anisotropic arrangement of elements

An energy relation in a model is suggested to evaluate the arrangements of elements in an environmental condition. Considering AuNPs arranged in a surface-coated free state or in a physically restricted interconnected state, the Helmholtz free energy (ΔF_{mix}) is evaluated in terms of the degree of interconnection of one component A (N_A) over another B (N_B) by increasing N_A/N_B from 1 to 1000 (Fig. S3). ΔF_{mix} corresponds to the maximum work performed at a constant temperature in a thermodynamic process. ΔF_{mix} of a lattice model is a function of the temperature (T), volume fraction of a component (ν), the dimensionless interaction parameter (χ) of the components and the Boltzmann constant (k),

$$\Delta F_{mix} = kT\left[\frac{\nu}{N_A}\ln(\nu) + \frac{(1-\nu)}{N_B}\ln(1-\nu) + \chi\nu(1-\nu)\right].$$

When one component becomes increasingly interconnected against the other (N_A/N_B) from 1 to 1000, $\Delta F_{mix}/kT$ significantly increases with a minimum or a maximum at a certain ν, at three different interaction parameters (χ = 1, 1.5 and 2). With increased incompatibility (increased χ from 1 to 2), $\Delta F_{mix}/kT$ significantly increases and the critical point changes from a minimum to a maximum at a ν (close to 0.4 on the graph) prominent at high N_A/N_B. Therefore, the degree of connection of one component A is more difficult when it is incompatible with the other component B.

For free components without linkages, the initial elongation needs more energy compared with the isotropic arrangement because it is against the thermodynamic rule of entropy increase. In addition, particulate interactions are modified by the compatibility of the particle surface with the environment. The graft chain length and the graft density modify the freedom of particulate components embedded in a less dense continuum (Akcora *et al.*, 2009). Assuming that the AuNP behaves as a single particle covered in brush-like grafts, self-assembly of the uniformly grafted particulates is investigated as a model system (see Section *Theoretical Analysis* in the supporting information). Due to the incompatibility of naked particle surfaces with the dispersing medium, particles without grafts form spherical clusters to minimize the contact area. There is a trade-off between the graft density and chain length due to space limitations on the particle surface. The increase in graft density generates an attractive interaction while the length of the chain contributes to a repulsive interaction of the particulates due to space filling and chain distortion. A short-range interparticle attraction is counterbalanced by the entropy increase which includes the graft chain distortion when the two particles approach each other. Minimization of free energy at a given state determines the assembly morphologies. In each morphology, the graft density and the graft chain length are inversely proportional [Fig. 5(*a*)]. As the graft chain length increases from N = 5 to N = 50 in accordance with the graft density decrease from 0.11 to zero, self-assembly changes from spherical aggregates, via cylindrical aggregates, to elongated lines before reaching a fully stretched network. At a given graft density on a particle (*i.e.* 0.09), the increased repulsion of the particles generated by the chain length increase leads to elongated morphologies. Meanwhile, at a fixed chain length (*i.e.* N = 35), an increase in graft density leads to elongated morphologies before it reaches the fully

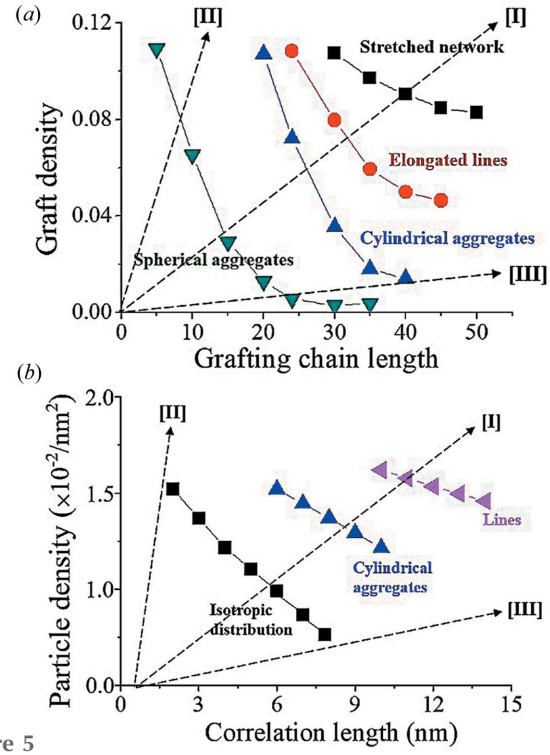

Figure 5
(*a*) Simulant results of graft density variation of AuNPs in accordance with the graft chain length, indicating a relation of attraction versus repulsion of particles. The structures transform from spherical aggregates to elongated lines when the graft chain length increases at a fixed graft density. Compared with line [I], where the two factors of graft density and chain length are balanced, deviation from this balanced condition, *e.g.* [II] and [III], moves away from anisotropic line patterns. (*b*) Experimentally obtained relationship between the particle density and the correlation length for the designed *f* (0, 50 and 70) with 2PEG10000 (×5). The result shows that the long correlation length matches with the observed elongated structure along with the increase in *f*. This is a similar tendency to the free graft particulate system shown in (*a*). Compared with the balanced line [I], the deviation of [II] and [III] moves away from the anisotropic line patterns.

stretched state. In the region where the graft density and chain length are properly balanced following the line [I], the morphology goes to elongated states. However, if it follows the unbalanced states like lines [II] and [III], there is no elongational arrangement. Therefore, a proper balance of the attraction and the repulsion is critical for line pattern formation.

Apart from the aforementioned free component behavior, an apparent line pattern formation of the network by repeatedly actuated swelling–deswelling procedure is affected by the continuum effect. The average particle density is experimentally related to the correlation length (ζ) in the designed nanocomposite (2PEG10000), where the AuNPs aggregate into various structures from isotropic, cylindrical to lined aggregates according to the *f* value increase (0, 50 and 70) [Fig. 5(*b*)]. The average particle density is a factor of particle attraction while ζ indicates a repulsive interaction. Increasing *f* increases ζ, experimentally confirmed by SAXS [Fig. 3(*a*)]. When the line follows the balanced region (line [I]), it goes from isotropic aggregates to elongated and further to lines. However, if it follows the unbalanced regions ([II] and [III]) it hardly reaches anisotropic patterns. This contributes dominantly to the long-range repulsion of nanoparticulates in a continuum, which is counterbalanced by the short-range attraction of nanoparticulate AuNPs generated by the chemical linkages in a continuum quantified by κ. The attraction versus repulsion profile of Fig. 5(*b*) displays a similar tendency to the surface grafted free particle system behavior in Fig. 5(*a*). Therefore, even with chemical linkages of the network, the particulates' behavior of the network structure is similar to free particulates in terms of the morphology control tendency. The line pattern formation is explained based on the force balance of repulsion and attraction.

3. Conclusion

In summary, repeated mechanical stress eventually produces an anisotropic linear structure of nanoparticulates rather than isotropy regardless of the source and direction of the forces. Responsive network assembly models are developed to verify the origin of the line patterns by tracing the junction movements. Various points are clarified from the model systems designed in this study. First, the distance between the nodal points in the network increases with increasing swelling–deswelling cyclic repetition (*f*) before it reaches a critical point. Second, the stress relaxation modulus $G(t)$ and critical threshold strain γ_{cr} are essential to drive anisotropic pattern formation. Based on the model system, the line patterning is accelerated by the stored energy when the stress is not completely relaxed during the cyclic repetition of mechanical swelling–deswelling. The presence of γ_{cr} indicates that only a sufficient amplitude of strain at each volume change step can generate line patterns. Third, non-directional (or isotropic) self-modulated strain change causes clustering of nanoparticulate components that are isotropic at the initial state. But these nanoparticulate clusters are eventually transformed into elongated lines and become longer by repeated mechanical actuations. From a bottom-up viewpoint, an equilibrium between the short-range attraction and long-range repulsion drives anisotropic orientation similar to the self-assembly of surface-modified free particulates. The findings in this study would contribute to a better understanding of the dynamic initiation of elastic instabilities naturally occurring in a broad range of biological systems and soft deformable materials. This technology can contribute to an effective design methodology of nanoscale patterned materials for a wide range of applications such as electrical devices and biomedical materials.

4. Methods

4.1. Gold nanoparticle incorporated nanocomposite preparation

A calculated amount of thiol functionalized polyethylene glycol (PEG) aqueous solution (see the supporting information) was mixed with prepared gold nanoparticle (AuNP) solution of AuNP average diameter 2 nm (2.4×10^{21}

AuNPs m^{-3}) at 90°C for 24 h. Binary thiol end-capped functional PEG molecules with molecular weight 3400 between the junction point (M_p) is expressed as 2PEG3400 [$(EO)_n$, $n = 77$], while binary PEG with 10000 M_p is 2PEG10000 [$(EO)_n$, $n = 227$], quaternary thiol end-capped functional PEG molecules with 10000 M_p is 4PEG10000 [$(EO)_n$, $n = 227$] and that with 20000 M_p is 4PEG20000 [$(EO)_n$, $n = 454$]. The products were purified to remove unreacted PEGs and AuNPs by membrane dialysis (Cellulose Ester, MW 20KDa cut, Spectra/Por®). The concentration of the ligand stock solution was varied as ×5, ×10 and ×20 of PEG/AuNP number ratio considering the multi-reactive sites on a single AuNP. Nanocomposites were concentrated in an aqueous solution which was not completely dried (hydrogel).

4.2. Small-angle X-ray scattering

Synchrotron SAXS analysis was performed at the 4C beamline of Pohang Light Source II (PLS II, Pohang, South Korea), equipped with a position-sensitive 2D detector. Two energy levels were employed for wavelength modulation: 10 keV (0.0675 nm^{-1}) and 18 keV (0.1217 nm^{-1}). A 1 mm-thick sample was prepared by stacking five 200 µm-thick Si wafers of the SiN_3 sample window (Ahn & Lee, 2015). A sample-to-detector distance (SDD) of 4 m covers the q range of 0.0679 $nm^{-1} < q < 1.64094$ nm^{-1}, where $q = (4\pi/\lambda)\sin(\theta/2)$ is the magnitude of the scattering vector and θ is the scattering angle. The q range was calibrated using polystyrene-*block*-poly(ethylene-*ran*-butylene)-*block*-polystyrene (SEBS, q = 0.19165 nm^{-1}). Conversely, an SDD of 1 m covers the q range of 0.346 $nm^{-1} < q < 7.68039$ nm^{-1}. This q range was calibrated using silver behenate (q = 1.052 nm^{-1}). A W/B_4C double multilayer monochromator was installed to deliver monochromatic X-ray beam with a wavelength of 6.75 nm (18360 keV) and spread of $\Delta\lambda/\lambda = 0.01$. The scattered X-rays were recorded by a CCD camera (CCD165; Mar CCD, Mar USA). The collected SAXS data were corrected by subtracting the background and empty cell scattering. q^* is the peak at the lowest position which indicates the structural frame only within which structure changes. The q_i ($i = 1, 2, 3, \ldots$) was designated for the peaks at the higher q region. These peaks indicate smaller scale structural information than q^*, indicating temperature-responsive network structure changes within a frame (q^*).

4.3. Synchrotron X-ray nanoscopy

Experiments were carried out at the 7C beamline at PLS II. To obtain focused images, monochromatic X-ray beam at 7 keV was focused on the sample using a condenser zone plate with 4 nm innermost and 100 nm outermost diameters (CZP, beryllium refractive compound lenses of 1 mm diameter). A stainless steel annular ring aperture (AA) with 2.4 mm inner and 3.2 mm outer diameters was used to obtain a hollow-cone type X-ray illumination on the sample for Zernike phase-contrast imaging. An order-sorting aperture composed of a tungsten plate was used not only to pass the focused beam but also to block the zeroth and higher-order diffracted X-rays. For phase-contrast imaging, a gold-plated ring-shaped phase plate (PP) array was placed downstream of the objective lens, and the ring dimensions (114.6 µm) were matched with that of the AA located at the CZP. For the experimental set-up with a large field of view, the CZP was removed to obtain the diverged beam on the sample. The thickness of the PP was approximately 0.7 µm, which corresponds to a λ/4 phase delay for positive phase contrast. The primary X-ray image was magnified 50 times by using an objective zone plate lens (140 µm innermost and 50 nm outermost diameter, W) and was converted into a visible image on a thin scintillator crystal (Tb:LSO, 20 µm thickness). The visible image was further magnified by ×20 using an optical microscope, providing a total magnification of ×1000 on a cooled CCD camera (Princeton Instrument VersArray 1300B cooled CCD) with a 1340 pixel × 1300 pixel resolution. This corresponds to an equivalent field-of-view of 21 µm × 21 µm in physical size.

Sample preparation followed the methods used in the previous reference (Ahn & Lee, 2015). A Si wafer holder with a SiN_3 membrane window at the center was used as a sample holder. After the sample loading on the SiN_3 membrane, the sample was sealed by another sample holder with Teflon O-ring spacer. The temperature-controlled experiments were performed in a humidity-controlled box (RH = 75%). The samples were taken out of the box only for the measurement. Since the X-rays pass through the SiN_3 window, the sealed samples were measured in the state between the two Si wafers (Fig. 6).

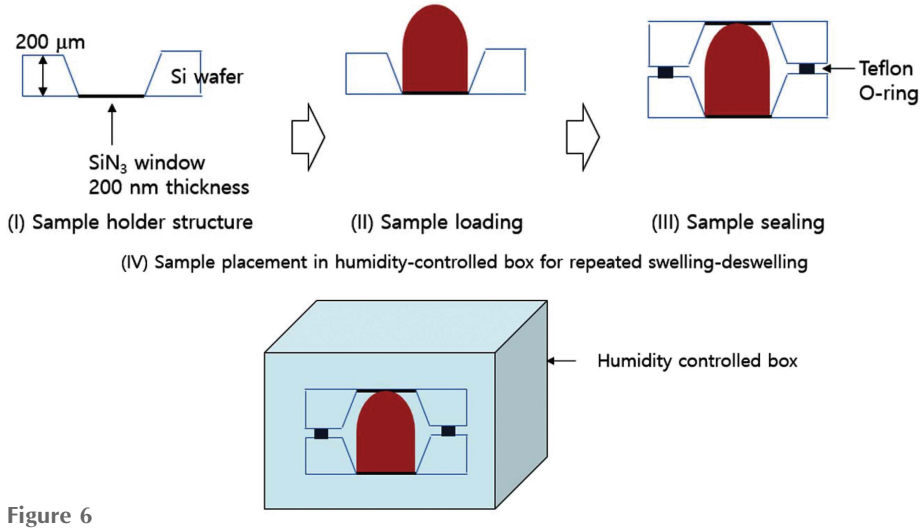

Figure 6
Sample preparation for synchrotron X-ray imaging and small-angle scattering. A Si wafer holder with a SiN_3 membrane window is used as a sample holder. After the sample loading it is sealed by another sample holder with Teflon O-ring spacer. The temperature-controlled experiments were performed in the humidity-controlled box.

4.4. Synchrotron X-ray microscopy

Synchrotron X-ray images were captured at the 6D beamline at PLS II. The X-ray source was a bending magnet of 8.7 keV at 3 GeV electron energy operation. The white beam was attenuated by polished beryllium (Be) of 0.5 mm thickness and polished Si wafer of 1 mm thickness. The photon energy (E) was about 22 keV with energy resolution ($\Delta E/E$) of 15.8 keV to 34.4 keV (∼84%). The brightness was ∼2 × 10^{12} photons s^{-1} mm^{-2} and the beam size was about 30 mm (H) × 5 mm (V). The sample was placed approximately 31 m downstream of the source, whereas the detector was placed 30 cm downstream of the objects. The size of the X-ray beam illuminating the sample was adjusted to that of the field of view by using a slit module to avoid unnecessary exposure of the X-ray beam on the sample. An attenuator made of polished silicon (Si) wafers was located at the beam inlet of the experiment hutch and on the pathway of X-ray propagation. This attenuation of light intensity protects the sample and detector from strong X-ray irradiation. The primary X-ray image was converted into a visible image on a thin $CdWO_4$ scintillator crystal of thickness 100 µm. X-ray images were captured using a CCD camera (Vieworks, VH-2MC). The field of view was approximately 11.8 mm × 8.8 mm in physical dimensions with a pixel size of about 7.4 µm.

Acknowledgements

The authors are grateful for the valuable help of the Pohang Light Source II (PLS II, Pohang, South Korea) in the synchrotron X-ray experiments of 4C SAXS, 6C XMI and 7C XNI. Further experimental specifics and additional experimental data are available free of charge via the authors or the Internet.

References

Ahn, S., Ahn, S. W. & Song, S. C. (2008). *J. Polym. Sci. B Polym. Phys.* **46**, 2022–2034.
Ahn, S. & Joon Lee, S. (2015). *Sci. Rep.* **5**, 11383.
Ahn, S., Jung, S. Y., Lee, J. P., Kim, H. K. & Lee, S. J. (2010). *ACS Nano*, **4**, 3753–3762.
Ahn, S. & Lee, S. J. (2014). *Sci. Rep.* **4**, 6624.
Ahn, S. & Lee, S. J. (2015). *Sci. Rep.* **5**, 7800.
Ahn, S., Monge, E. C. & Song, S. C. (2009). *Langmuir*, **25**, 2407–2418.
Akcora, P., Liu, H., Kumar, S. K., Moll, J., Li, Y., Benicewicz, B. C., Schadler, L. S., Acehan, D., Panagiotopoulos, A. Z., Pryamitsyn, V., Ganesan, V., Ilavsky, J., Thiyagarajan, P., Colby, R. H. & Douglas, J. F. (2009). *Nat. Mater.* **8**, 354–359.
Bae, H. J., Bae, S., Park, C., Han, S., Kim, J., Kim, L. N., Kim, K., Song, S. H., Park, W. & Kwon, S. (2015). *Adv. Mater.* **27**, 2083–2089.
Belkin, M., Snezhko, A., Aranson, I. S. & Kwok, W. K. (2007). *Phys. Rev. Lett.* **99**, 158301.
Cao, Y. P. & Hutchinson, J. W. (2012). *J. Appl. Mech.* **79**, 031019.
Cerda, E. & Mahadevan, L. (2003). *Phys. Rev. Lett.* **90**, 074302.
Cerda, E., Ravi-Chandar, K. & Mahadevan, L. (2002). *Nature*, **419**, 579–580.
Chen, X. & Hutchinson, J. W. (2004). *J. Appl. Mech.* **71**, 597–603.
Ciarletta, P., Destrade, M. & Gower, A. L. (2013). *Q. J. Mech. Appl. Math.* **66**, 273–288.
Danov, K. D., Kralchevsky, P. A. & Stoyanov, S. D. (2010). *Langmuir*, **26**, 143–155.
Destrade, M., Gilchrist, M. D., Motherway, J. A. & Murphy, J. G. (2010). *Mech. Mater.* **42**, 469–476.
Efimenko, K., Rackaitis, M., Manias, E., Vaziri, A., Mahadevan, L. & Genzer, J. (2005). *Nat. Mater.* **4**, 293–297.
Falconer, K. (2014). *Fractal Geometry: Mathematical Foundations and Applications*, 3rd ed. Wiley & Sons.
Fejer, S. N., Chakrabarti, D. & Wales, D. J. (2011). *Soft Matter*, **7**, 3553.
Freitas, G., Magee, C., Dardzinski, P. & Fusco, T. (1994). *Adv. Mater.* **25**, 36–43.
Golubitsky, M., Stewart, I., Buono, P.-L. & Collins, J. J. (1999). *Nature*, **401**, 693–695.
Gupta, S., Zhang, Q. L., Emrick, T., Balazs, A. C. & Russell, T. P. (2006). *Nat. Mater.* **5**, 229–233.
Hohlfeld, E. (2008). PhD thesis, Harvard University, Cambridge, MA, USA.
Huang, Z. Y., Hong, W. & Suo, Z. (2005). *J. Mech. Phys. Solids*, **53**, 2101–2118.
Kammler, H. K., Beaucage, G., Mueller, R. & Pratsinis, S. E. (2004). *Langmuir*, **20**, 1915–1921.
Kondo, S. & Miura, T. (2010). *Science*, **329**, 1616–1620.
Koo, W. H., Jeong, S. M., Araoka, F., Ishikawa, K., Nishimura, S., Toyooka, T. & Takezoe, H. (2010). *Nat. Photon.* **4**, 222–226.
Li, C., Zhang, X. & Cao, Z. (2005). *Science*, **309**, 909–911.
Livio, M. (2003). *The Golden Ratio: The Sstory of Phi, The World's Most Astonishing Number.* Reprint edition. New York: Broadway Books.
Maini, P. K., Baker, R. E. & Chuong, C. M. (2006). *Science*, **314**, 1397–1398.
Mansfield, E. H. (1968). *Proceedings of the XIIth International Congress on Theoretical and Applied Mechanics.* New York: Springer-Verlag.
Mariotti, G., Pruss, S. B., Perron, J. T. & Bosak, T. (2014). *Nat. Geosci.* **7**, 736–740.
Mortensen, A. & Suresh, S. (1995). *Int. Mater. Rev.* **40**, 239–265.
Ogawa, K., Vogt, T., Ullmann, M., Johnson, S. & Friedlander, S. K. (2000). *J. Appl. Phys.* **87**, 63–73.
Ostling, A., Harte, J. & Green, J. (2000). *Science*, **290**, 671.
Pocivavsek, L., Dellsy, R., Kern, A., Johnson, S., Lin, B., Lee, K. Y. C. & Cerda, E. (2008). *Science*, **320**, 912–916.
Rabani, E., Reichman, D. R., Geissler, P. L. & Brus, L. E. (2003). *Nature*, **426**, 271–274.
Richman, D. P., Stewart, R. M., Hutchinson, J. W. & Caviness, V. S. (1975). *Science*, **189**, 18–21.
Sciortino, F., Bianchi, E., Douglas, J. F. & Tartaglia, P. (2007). *J. Chem. Phys.* **126**, 194903.
Seul, M. & Andelman, D. (1995). *Science*, **267**, 476–483.
Sillitoe, R. H. (1974). *Nature*, **250**, 542–545.
Steigmann, D. J. (1990). *Proc. R. Soc. London A*, **429**, 141–173.
Summers, B. (2013). *Nature*, **16**, 12175.
Tang, Z., Zhang, Z., Wang, Y., Glotzer, S. C. & Kotov, N. A. (2006). *Science*, **314**, 274–278.
Wagner, H. (1929). *Z. Flugtech. Motorluftschiffart*, **20**, 8–12.
Yin, J., Yagüe, J. L., Eggenspieler, D., Gleason, K. K. & Boyce, M. C. (2012). *Adv. Mater.* **24**, 5441–5446.
Zhuang, W. Z. & Halford, G. R. (2001). *Int. J. Fatigue*, **23**, 31–37.